Augmenting GNSS PPP Accuracy in South China Using Water Vapor Correction Data from WRF Assimilation Results

Yangzhao Gong[1], Zhizhao Liu[2], Pak Wai Chan[3], Kai Kwong Hon[4]

Abstract. Wet delay in Global Navigation Satellite System (GNSS), mainly caused by water vapor in the atmosphere, is difficult to be accurately modeled using empirical wet delay models as water vapor is highly variable in both space and time. In this paper we propose correcting the GNSS wet delay using water vapor data from Weather Research and Forecasting (WRF) model's assimilation results. We conduct six consecutive 24-h WRF forecasts to model the three-dimension (3D) distribution of water vapor in the South China region 20° N – 33° N and 108° E – 123° E from 0 h UTC April 06, 2020 to 0 h UTC April 11, 2020. GNSS Precipitable Water Vapor (PWV) from 27 stations of the Crustal Movement Observation Network of China (CMONOC) and meteorological profiles from 22 radiosonde stations are assimilated into WRF model to improve the water vapor modeling performance of WRF. Totally, four WRF schemes are adopted, i.e. WRF scheme 0: WRF without water vapor data assimilation; WRF scheme 1: WRF with GNSS PWV assimilation only; WRF scheme 2: WRF with radiosonde profiles assimilation only; WRF scheme 3: WRF with both GNSS PWV and radiosonde profiles assimilation.

The water vapor data from the four WRF schemes are used to augment Precise Point Positioning (PPP) by correcting GNSS wet delay at seven International GNSS Service (IGS) stations distributed in South China. The static PPP results show that using the water vapor correction data from different WRF schemes can

[1] Yangzhao Gong
Department of Land Surveying & Geo-Informatics (LSGI), The Hong Kong Polytechnic University (PolyU), Kowloon, Hong Kong, P. R. China
Research Institute for Sustainable Urban Development, The Hong Kong Polytechnic University (PolyU), Kowloon, Hong Kong, P. R. China

[2] Zhizhao Liu (✉)
Department of Land Surveying & Geo-Informatics (LSGI), The Hong Kong Polytechnic University (PolyU), Kowloon, Hong Kong, P. R. China
Research Institute for Sustainable Urban Development, The Hong Kong Polytechnic University (PolyU), Kowloon, Hong Kong, P. R. China
e-mail: lszzliu@polyu.edu.hk

[3] Pak Wai Chan
The Hong Kong Observatory, Kowloon, Hong Kong, P. R. China

[4] Kai Kwong Hon
The Hong Kong Observatory, Kowloon, Hong Kong, P. R. China

improve PPP positioning accuracy by 29.5% to 42.3% in the vertical component of GNSS stations. In addition, the WRF-augmented PPP can shorten convergence time by 43.3% to 57.3% in the GNSS station vertical component, if using 10 cm positioning error as the convergence criterion. The kinematic PPP results show that WRF-augmented PPP can improve positioning accuracy in the vertical component by 20.0% to 33.6%.

Keywords: Global Navigation Satellite System (GNSS) · Weather Research and Forecasting (WRF) Model · Data Assimilation · Precipitable Water Vapor (PWV) · Precise Point Positioning (PPP).

1 Introduction

GNSS Precise Point Positioning (PPP) is a capable positioning technique that can use a single GNSS receiver to determine receiver's coordinates with a accuracy level of centimetre even sub-centimetre [1–3]. Different from differential GNSS positioning method, PPP cannot utilize GNSS observations from neighbouring receivers to mitigate errors, such as tropospheric wet delay. Therefore, how to mitigate the impacts of wet delay in PPP has long been a research topic in the GNSS community.

One widely used method is to treat wet delay as an unknown parameter and estimate wet delay in parallel with receiver coordinates, receiver clock offset and other parameters [1]. This method normally needs at least 30 min to achieve centimetre level of coordinate solutions [4–6].

Another method is to correct wet delay directly using external water vapor information [7–9]. For this method, the positioning accuracy highly depends on the accuracy of external water vapor information used. Normally, the external water vapor can be from empirical tropospheric delay models, regional GNSS network, collocated water vapor observation systems, Numerical Weather Prediction (NWP) models and others.

Using empirical tropospheric delay models to correct wet delay is a simple and convenient way to mitigate the wet delay in PPP. This method has been widely adopted in many studies [10–12]. However, due to the low accuracy of wet delay derived from the empirical tropospheric delay models, the PPP positioning accuracy in vertical component is normally over 10 cm while the horizontal component normally is less affected by atmospheric wet delay [12, 13].

Several studies obtained wet delay corrections from regional GNSS network [14–16]. These studies proved that convergence speed and positioning accuracy can be improved by using tropospheric delay information from regional tropospheric delay models. However, in order to obtain accurate regional tropospheric delay corrections, a dense GNSS network is needed.

Using water vapor information from other collocated observation systems can also improve GNSS positioning performance [9, 17]. However, normally no collocated water vapor observation system is available at most GNSS stations.

In the recent years, the accuracy and spatial resolution of NWP model has undergone a significant improvement [18, 19]. NWP model has been used to correct wet delay for GNSS positioning [7, 20–22]. For example, Lu et al. [7] used ZWD from a global NWP model, i.e., the Global Forecast System (GFS) of the National Centers for Environmental Prediction (NCEP), to improve BDS real-time positioning performance. In their study, the ZWD from NCEP was treated as a priori ZWD value and the ZWD residual was treated as the unknow parameter to be estimated. The PPP results at more than 30 globally distributed International GNSS Service (IGS) stations showed that NCEP-augmented PPP can shorten convergence time up to 60.0% and 66.7% in east and up components, respectively, compared with standard PPP results. Additionally, NCEP-augmented PPP improved positioning accuracy in east, north, and up components by around 40%, 50%, and 30%-40%, respectively. Wilgan et al. [22] conducted an experiment using high spatial resolution (4 km) Weather Research and Forecasting (WRF) model to augment GNSS real time PPP. Their experiment results showed that WRF-augmented real time kinematic PPP reduced the convergence time from 67 min to 58 min to achieve an accuracy of 10 cm level in horizontal component and from 79 min to 63 min in vertical component. These studies demonstrated that PPP performance can be improved using the water vapor augmentation information from NWP models. However, Global NWP products have a low spatial resolution. For example, the spatial resolution of advanced global NWP reanalysis product, ECMWF Reanalysis v5 (ERA5), can only reach 31 km [23]. For WRF model, its modeling results can have a high spatial resolution. In addition, WRF has a data assimilation system that can assimilate external meteorological observations to improve WRF weather modeling performance [24, 25]. However, very few studies have investigated the benefits of WRF data assimilation for PPP augmentation.

In this study, the state-of-the-art NWP model, WRF model, was used to provide wet delay corrections to improve PPP performance in South China region. To further improve the accuracy of water vapor from WRF model, we assimilated two sets of water vapor data into the WRF model. One is the water vapor data from 27 GNSS stations of the Crustal Movement Observation Network of China (CMONOC) and the other is the meteorological profiles from 22 radiosonde stations in the South China region. The data were assimilated into WRF model in four different assimilation schemes, as shown in Table 1, i.e. WRF scheme 0: WRF without data assimilation; WRF scheme 1: WRF with assimilation of GNSS PWV only; WRF scheme 2: WRF with assimilation of radiosonde profiles only; WRF scheme 3: WRF with assimilation of both GNSS PWV and radiosonde profiles.

Table 1 WRF schemes and the data to be assimilated

WRF scheme no.	Data assimilated
WRF 0	-
WRF 1	GNSS PWV
WRF 2	Radiosonde profiles
WRF 3	GNSS PWV + radiosonde profiles

In order to assess the accuracy of the water vapor results from the four different WRF schemes, the WRF water vapor modeling results are first validated by PWV data from GNSS stations. Then, the WRF water vapor data are utilized to augment PPP performance at seven IGS stations distributed in South China by correcting wet delay in GNSS signals. This also allows the assessment of the performance of WRF modeling via the examination of the PPP accuracy [17].

The remaining paper is organized as follows. In Section 2, the WRF configuration and the methods used to retrieve WRF PWV are described. In Section 3, the data assimilated, namely CMONOC GNSS PWV and radiosonde profiles, and the IGS GNSS observations used in PPP validation are introduced. In Section 4, the WRF PWV are evaluated by PWV from 27 CMONOC GNSS stations. In Section 5, WRF wet delay are used to augment GNSS PPP at seven IGS stations and the WRF-augmented PPP results are analyzed. In Section 6, the conclusions are summarized.

2 Description of WRF Experiment

2.1 WRF Configuration

WRF model is an advanced NWP model and has been widely used in various research fields, such as weather simulation [26], climate change forecasting [27], as well as geodetic surveying [22]. Based on the initial weather conditions, WRF can model or forecast the variation of meteorological parameters including water vapor field, for the following multiple days or even longer.

In this study, WRF with Advanced Research WRF (ARW) core version 4.2 was used. Two two-way nested domains were adopted to cover the South China area around 20° N – 33° N and 108° E – 123° E. The locations of two WRF domains are shown in Fig. 1. Six consecutive 24-h WRF forecasts, i.e. WRF forecasts 1 to 6, were initialized at 0 h UTC on April 06 to April 11, 2020, respectively. The ECMWF ERA5 reanalysis products were used as the initial conditions and boundary conditions for the WRF model in this experiment. The spatial structure of WRF model set and microphysics options adopted in this WRF model are shown in Table 2.

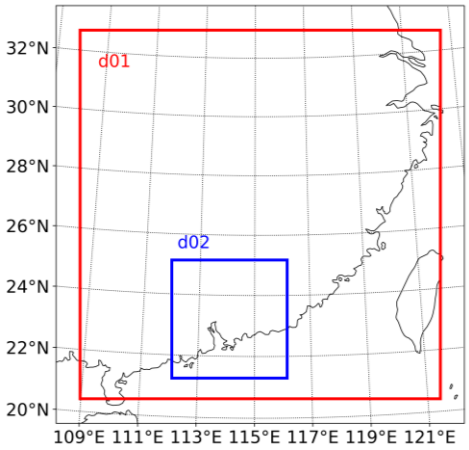

Fig. 1 The locations of two WRF modeling domains used in this study. d01 (red) and d02 (blue) denote the WRF domain 01 and domain 02, respectively. The WRF grid spacings of domain 01 and domain 02 are 9 km and 3 km, respectively

Table 2 Design and configuration of WRF model

	domains	
	domain 01	domain 02
Number of grid point (North-South×East-West)	154×157	148×151
Grid spacing	9 km	3 km
Number of WRF layers	33	33
Model top pressure	50 hPa	50 hPa
Cumulus parameterization	Kain-Fritsch [28]	-
Longwave radiation	RRTMG longwave scheme [29]	RRTMG longwave scheme [29]
Shortwave radiation	RRTMG shortwave scheme [29]	RRTMG shortwave scheme [29]
Planetary boundary layer	Yonsei university scheme [30]	Yonsei university scheme [30]
Surface layer	Revised MM5 scheme [31]	Revised MM5 scheme [31]
Land surface	5–layer thermal diffusion scheme [32]	5–layer thermal diffusion scheme [32]

To improve WRF water vapor modeling performance, GNSS PWV and radiosonde meteorological profiles were assimilated into WRF model domain 01 and domain 02 at the WRF initial time (0 h UTC, April 06 to April 11, 2020) .

WRF 3DVAR data assimilation method was used since 3DVAR can assimilate external data effectively with less computational burden compared to WRF 4DVAR [24]. To investigate the impacts resulting from different WRF data assimilation schemes, four WRF schemes were studied in this paper, as shown in Table 1.

2.2 Retrieval of ZWD and PWV Based on WRF Outputs

WRF model can provide modeling results of various meteorological variables including mixing ratio of vapor, air potential temperature, air base state pressure, air perturbation pressure. These output variables can be used to calculate ZWD using the following formulas. First, the water vapor mixing ratio (Q, unit: kg·kg^{-1}) can be converted to water vapor partial pressure (e, unit: hPa) [33]:

$$e = \frac{P \cdot Q}{0.622 + Q} \tag{1}$$

where P is the air total pressure in unit of hPa, which is the sum of air base state pressure and perturbation pressure:

$$P = P_{base} + P_{per} \tag{2}$$

where P_{base} and P_{per} are the air base state pressure and perturbation pressure, respectively, both in unit of hPa.

Then the atmosphere wet refractivity Nw can be calculated as follows [34]:

$$N_w = \left(k_2 - k_1 \frac{R_d}{R_w}\right) \frac{e}{T} + k_3 \frac{e}{T^2} \tag{3}$$

where R_d = 287.053 J·K^{-1}·kg^{-1} and R_w = 461.495 J·K^{-1}·kg^{-1} are the gas constants for dry air and water vapor, respectively. T is the air temperature in unit of Kelvin. k_1 = 77.6890 K/hPa, k_2 = 71.2952 K/hPa, k_3 = 375463 K^2/hPa are refractivity constants [35].

The formula used to convert air total potential temperature to air temperature can be expressed as [33]:

$$T = (T_\theta + 300) \left(\frac{P}{1000}\right)^{\frac{R_d}{cp}} \tag{4}$$

where T_θ denotes the potential temperature in unit of Kelvin. P refers to the air pressure in unit of hPa. R_d has been defined in formula (3). c_p is the specific heat capacity at a constant pressure. The ratio of R_d and c_p, i.e. R_d/c_p = 2/7, is the Poisson constant.

Finally, the WRF ZWD can be derived using [34]:

$$ZWD = 10^{-6} \int_{h_s}^{\infty} N_w(h)\, dh \tag{5}$$

where h is the height of layer in unit of meter.

WRF ZWD can be converted to PWV using a PWV conversion factor (PWV_{factor}) [36]:

$$PWV = ZWD \times PWV_{factor} \tag{6}$$

$$PWV_{factor} = \frac{10^5}{461.495\left(k_2 - k_1\frac{M_w}{M_d} + \frac{k_3}{T_m}\right)} \quad (7)$$

where k_1, k_2, k_3 have been defined in formula (3). M_w = 0.018016 kg/mol and M_d = 0.028964 kg/mol are the molar mass of water vapor and dry air, respectively. T_m represents the weighted temperature in unit of Kelvin.

T_m can be calculated using an empirical model [37]:

$$T_m = 70.2 + 0.72\ T_s \quad (8)$$

where T_s is the temperature near the Earth surface in unit of Kelvin. In this study, T_s is retrieved from ERA-5 single pressure reanalysis product.

3 Description of Data

3.1 Data Assimilated

3.1.1 CMONOC GNSS PWV

A total of 27 China CMONOC GNSS stations, as shown in Fig. 2, are used to generate PWV for this study. The PWV are then assimilated into WRF model according to the designed WRF schemes. The CMONOC GNSS PWV data are extracted directly from the troposphere products of China Earthquake Administration [38]. GAMIT/GLOBK positioning software is adopted to generate this troposphere product using differential positioning method [39]. For this troposphere product, tropospheric delay is estimated as an unknown parameter in hourly intervals. The PWV from 27 CMONOC GNSS stations are assimilated into WRF model at WRF initial time. After the WRF model forecasts water vapor data for the next 1 h to 24 h, the CMONOC GNSS PWV are also used to validate these results, as shown in Section 4. It should be noted that, PWV data at the GNSS station (27.9° N, 109.8° E) are missing at data assimilation time point (0 h UTC) from April 06 to April 09, 2020. The number of GNSS PWV assimilated for each day from April 06 to April 11, 2020 has been listed in Table 3.

3.1.2 Radiosonde Profiles

Radiosonde meteorological profiles used in this study are obtained from the Integrated Global Radiosonde Archive (IGRA). Currently, IGRA provides radiosonde profile records at more than 1000 globally distributed radiosonde stations. Normally two profiles are observed at each station at 0 h and 12 h UTC

per day. In this study, meteorological profiles, i.e. relative humidity, temperature, and pressure profiles from 22 IGRA radiosonde stations, are assimilated into WRF model. The distribution of 22 radiosonde stations is also shown in Fig. 2. Also, data from several radiosonde are missing at 0 h UTC from April 06 to April 11, 2020. The detailed number of radiosonde profiles assimilated on each day from April 06 to April 11, 2020 is shown in Table 3.

Table 3 Number of GNSS PWV observations and radiosonde profiles assimilated for each day from April 06 to April 11, 2020.

Date (April 2020)	06	07	08	09	10	11
GNSS	26	26	26	26	27	27
Radiosonde	21	17	18	10	15	17

3.2 IGS GNSS Observations in PPP Experiment

GNSS observations with sampling rate of 30 seconds from seven IGS stations were used to conduct PPP experiment to evaluate the WRF-generated PWV data. The locations of seven IGS stations are displayed in Fig. 2 and the type of GNSS receivers for seven IGS stations are listed in Table 4. Only GPS observations were used in PPP in this study.

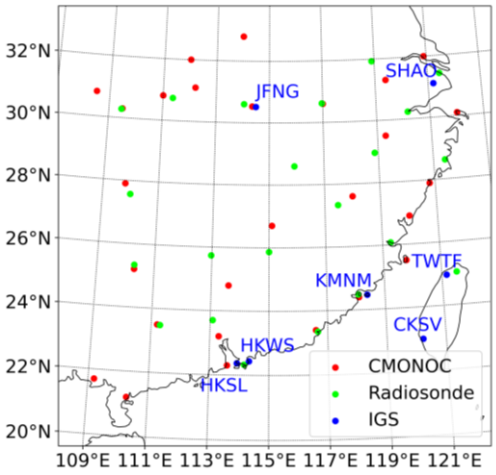

Fig. 2 The distribution of 27 CMONOC GNSS stations (red dots), 17 radiosonde stations (green dots), and 7 IGS GNSS stations (blue dots) used in this study. PWV from CMONOC GNSS stations were first assimilated into WRF model and then used to validate WRF PWV forecasting

results. Radiosonde profiles were assimilated into WRF model. IGS GNSS observations were used in PPP validation

Table 4 The type of GNSS receivers at seven IGS stations used in PPP validation

IGS station	Type of GNSS receiver
CKSV	TRIMBLE ALLOY
HKSL	LEICA GR50
HKWS	LEICA GR50
JFNG	TRIMBLE NETR9
KMNM	TRIMBLE ALLOY
SHAO	ASHTECH UZ-12
TWTF	SEPT POLARX4

4 Validation of WRF PWV

With the four designed WRF schemes, we can output the PWV from the WRF forecasting model. We forecast the WRF PWV every hour with lead time from 1 h to 24 h (lead time of 1 h to 24 h for WRF forecasts 1 to 6: 1 h UTC to 24 h UTC, April 06 to 11, 2020). The WRF forecasting PWV from different WRF schemes are evaluated by China CMONOC GNSS PWV.

Fig. 3 shows the hourly PWV RMSE of different WRF schemes at different WRF lead time. We can find that the PWV RMSE of those WRF schemes with assimilation of GNSS PWV (WRF schemes 1 and 3) within the first 5-7 h are evidently smaller than that of WRF without data assimilation (WRF scheme 0). This implies that assimilating GNSS PWV improves the initial water vapor information in WRF model, leading to better forecasting output. It also shows that assimilating radiosonde profiles (WRF scheme 2) has a limited impact in PWV RMSE in comparison with GNSS PWV. When WRF forecasting lead time is more than 7 hours, we can see that all the four WRF schemes have very similar performances.

The PWV RMSE of different WRF schemes within the first 7 h forecasting are summarized in Table 5. As we can see, within the first 7 h, the average PWV RMSE of WRF scheme 0 for three WRF forecasts is 2.3 kg/m^2. Assimilation of GNSS PWV improves the WRF water vapor forecasting results. The average PWV RMSE for WRF schemes 1, 2, 3 are 1.9 kg/m^2, 2.3 kg/m^2 and 2.0 kg/m^2, respectively. This means an improvement of up to 17.4% in accuracy of water vapor forecasting performance due to data assimilation.

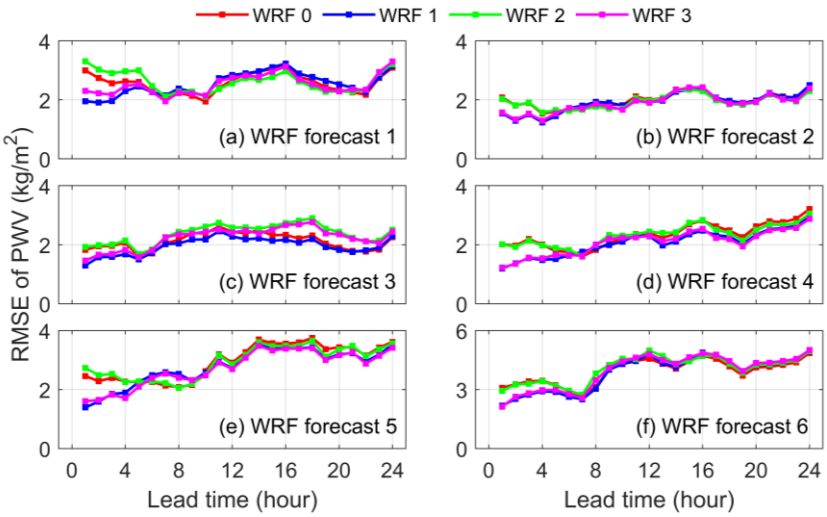

Fig. 3 The hourly PWV RMSE of four WRF schemes evaluated by 27 China CMONOC GNSS PWV at WRF lead time of 1 h to 24 h for WRF forecasts 1-6. WRF forecasts 1-6 are six consecutive 24-h WRF forecasts initialized at 0 h UTC from April 06 to 11, 2020, respectively. Lead time of 1 h to 24 h for WRF forecast 1 to 6: 1 h UTC – 24 h UTC, April 06 to 11, 2020.

Table 5 The PWV RMSE of four WRF schemes (WRF schemes 0-3) evaluated by 27 China CMONOC GNSS PWV within the first 7 h for WRF forecasts 1-6. WRF forecasts 1-6 are six consecutive 24-h WRF forecasts initialized at 0 h UTC, from April 06 to 11, 2020, respectively. The percentage denotes the RMSE reduction of WRF with data assimilation (WRF schemes 1-3) compared with WRF without data assimilation (WRF scheme 0). Negative/ positive percentage means an RMSE decrease/increase in PWV forecasting accuracy. Unit of PWV RMSE: Unit: kg/m^2

	WRF scheme 0	WRF scheme 1	WRF scheme 2	WRF scheme 3
WRF forecast 1	2.6	2.1 (-19.2%)	2.8 (7.7%)	2.3 (-11.5%)
WRF forecast 2	1.8	1.5 (-16.7%)	1.8 (0%)	1.5 (-16.7%)
WRF forecast 3	1.9	1.6 (-15.8%)	2.0 (5.3%)	1.8 (-5.3%)
WRF forecast 4	1.9	1.5 (-21.1%)	1.9 (0%)	1.5 (-21.1%)
WRF forecast 5	2.3	2.0 (-13.0%)	2.4 (4.3%)	2.0 (-13.0%)
WRF forecast 6	3.1	2.6 (-16.1%)	3.1 (0%)	2.7 (-12.9%)
Average	2.3	1.9 (-17.4%)	2.3 (0%)	2.0 (-13.0%)

5 Augmenting PPP with PWV Data from WRF Forecasting

5.1 PPP Strategies

In this study, we aim to augment PPP performance through the use of PWV data from each WRF data assimilation scheme. At the same time, we can evaluate the PPP accuracy of each WRF assimilation scheme. Two PPP processing strategies are adopted. For the first PPP strategy, a prior tropospheric wet delay is calculated using Saastamoinen model [40] based on the standard meteorological parameters (relative humidity: 50%, air temperature: 15°C, air pressure: 1013.25 hPa) [41]. The tropospheric wet delay residual is then estimated as an unknown parameter with a spectral density of 3×10^{-8}. This PPP method is the traditional PPP method and is denoted as "Estimated" PPP in this study. Another PPP strategy is using wet delay corrections derived from WRF model to correct PPP wet delay directly. In these two strategies, the tropospheric dry delay is corrected using the same method, which are calculated using Saastamoinen dry delay model [40] based on the pressure data from ECMWF ERA5 single pressure reanalysis product. The ratio between pseudorange observation standard deviation and carrier phase observation standard deviation is set to 100:1. In addition, an elevation-dependent weighting strategy is used to determine weight for pseudorange and carrier phase observations.

As shown in Fig. 3, the assimilation of GNSS PWV and radiosonde profiles mainly improves the WRF water vapor forecasting within the first 5-7 hours. Therefore we conduct PPP test within the first 7 h of WRF lead time only. The cutoff angle of GNSS observations used in PPP is set to 10°. The daily static PPP coordinate solutions using Bernese positioning software version 5.2 are treated as the benchmark coordinates [41].

5.2 PPP Results with Wet Delay Corrections from WRF Domain 01

5.2.1 Static and Kinematic PPP Positioning Accuracy

In this section, the wet delay corrections from WRF forecasting in geographic domain 01 are used to augment the performance of static and kinematic PPP. We did the RMSE statistics with the PPP positioning errors. The PPP usually needs to take approximately half an hour to get GNSS carrier phase ambiguities resolved [42]. In this study we thus only analyze the positioning results after GNSS carrier phase ambiguities have converged. Given that the first portion of PPP results have

large positioning errors, we selected PPP results only in the period from 2 h to 7 h UTC over April 06 to 11, 2020. The 6-day average RMS of static PPP positioning errors in east, north, and up components and overall three-dimension (3D) for each IGS station are shown in Fig. 4. As we can see, compared with "Estimated" static PPP results, the RMS of positioning errors of all WRF-augmented static PPP in the up component are smaller at most IGS stations. In contrast, no improvement or even slight degradation is found in horizontal positioning accuracy of WRF-augmented PPP. We can also notice that the WRF-augmented PPP positioning results at station SHAO are much worse than that of "Estimated" PPP. One potential reason could be that station SHAO is geographically located near the edge of WRF domain 01, where WRF may have a poor forecasting performance.

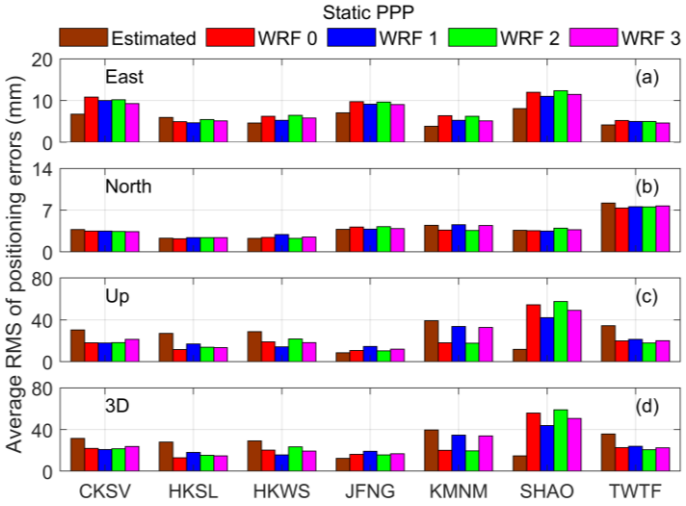

Fig. 4 6-day average RMS of positioning errors in east, north, and up components and overall 3D for traditional "Estimated" static PPP scheme and four WRF-augmented static PPP schemes at seven IGS stations during April 06 to 11, 2020. Only the positioning results from 2 h to 7 h UTC for each day are used in RMS statistics

The average RMS of positioning errors for seven IGS stations for April 06–11, 2020 are summarized in Table 6. To avoid the significant statistical errors introduced by the special case, the positioning results at IGS station SHAO are excluded in statistics. Table 6 indicates that WRF-augmented static PPP improves the PPP 3D positioning accuracy significantly. The WRF schemes 0 to 3 improve the PPP 3D positioning accuracy by 35.4%, 24.8%, 34.0%, and 25.5%, respectively, in comparison with traditional static PPP method where the water vapor error is "Estimated" as one unknown parameter.

The WRF schemes augment the up component more prominently than the horizontal one. In the up component, the traditional "Estimated" PPP has an RMSE error of 28.1 mm. This RMSE reduces to 16.2 mm, 19.8 mm, 16.7 mm,

and 19.7 mm, respectively, after applying the water vapor data from WRF schemes 0 to 3. This suggests an improvement of 42.3%, 29.5%, 40.6%, and 29.9% in up component for the WRF schemes 0-3, respectively. Nevertheless, the WRF-augmented PPP's positioning results have a degradation in the horizontal component, particularly in east component. Despite the degradation in horizontal component, the overall 3D positioning accuracy after the WRF augmentation still show an improvement of 24.8% to 35.4%, as shown in Table 6.

Table 6 Average RMS of static PPP positioning errors in east, north, and up components and overall 3D based on the positioning results at seven IGS stations during April 06 to 11, 2020. Only the positioning results during 2 h to 7 h UTC for each day are used in statistics. The percentage denotes the error reduction of each WRF-augmented PPP (WRF schemes 0-3) compared with traditional "Estimated" PPP. Negative/positive percentage means an RMS decrease/increase in positioning errors. Unit of positioning error: mm

	Estimated static PPP	WRF scheme 0	WRF scheme 1	WRF scheme 2	WRF scheme 3
East	5.4	7.2 (33.3%)	6.5 (20.4%)	7.2 (33.3%)	6.5 (20.4%)
North	4.1	3.9 (-4.9%)	4.1 (0%)	3.9 (-4.9%)	4.1 (0%)
Up	28.1	16.2 (-42.3%)	19.8 (-29.5%)	16.7 (-40.6%)	19.7 (-29.9%)
3D	29.4	19.0 (-35.4%)	22.1 (-24.8%)	19.4 (-34.0%)	21.9 (-25.5%)

The 6-day average kinematic PPP positioning errors in east, north, and up components and overall 3D for each IGS station are shown in Fig. 5. Similar to static PPP results, all WRF-augmented kinematic PPP schemes show a smaller positioning error in the up component compared with the traditional kinematic PPP ("Estimated" PPP). The average kinematic PPP positioning errors for seven IGS stations using different PPP schemes are shown in Table 7. The kinematic positioning results for IGS station SHAO are also excluded in kinematic PPP accuracy statistics for the same reason stated above. We can see that, compared with "Estimated" kinematic PPP, WRF-augmented PPP schemes 0 to 3 improve the positioning accuracy in up component by 33.3%, 21.5%, 33.6%, and 20.0%, respectively. For 3D positioning accuracy, the corresponding improvements for WRF-augmented PPP schemes 0 to 3 are 25.5%, 14.8%, 26.3%, and 14.8%, respectively.

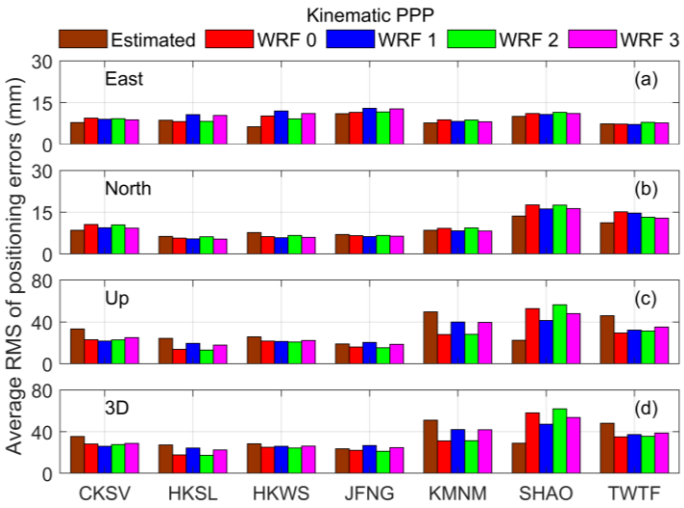

Fig. 5 6-day average RMS of positioning errors in east, north, and up components and overall 3D for traditional "Estimated" kinematic PPP scheme and four WRF-augmented kinematic PPP schemes at seven IGS stations for April 06-11, 2020. Only the positioning results from 2 h to 7 h UTC for each day are used in RMS statistics

Table 7 Average RMS of kinematic PPP positioning errors in east, north, and up components and overall 3D based on the positioning results at seven IGS stations from April 06 to 11, 2020. Only the positioning results during 2 h to 7 h UTC for each day are used in statistics. The percentage denotes the error reduction of each WRF-augmented PPP (WRF schemes 0-3) compared with the traditional "Estimated" PPP. Negative/positive percentage means an RMS decrease/increase in positioning errors. Unit of positioning error: mm

	Estimated kinematic PPP	WRF scheme 0	WRF scheme 1	WRF scheme 2	WRF scheme 3
East	8.1	9.2 (13.6%)	10.0 (23.5%)	9.1 (12.3%)	9.8 (21.0%)
North	8.2	8.9 (8.5%)	8.3 (1.2%)	8.7 (6.1%)	8.0 (-2.4%)
Up	33.0	22.0 (-33.3%)	25.9 (-21.5%)	21.9 (-33.6%)	26.4 (-20.0%)
3D	35.7	26.6 (-25.5%)	30.4 (-14.8%)	26.3 (-26.3%)	30.4 (-14.8%)

We notice that WRF-augmented PPP scheme 0 (without data assimilation) even has a positioning accuracy better than WRF-augmented PPP with data assimilation (WRF schemes 1-3). However, we find PWV from WRF with data assimilation have a smaller RMSE when evaluated by GNSS PWV as shown in Section 4. This could be explained as follows. Assimilating external water vapor data into WRF model at WRF initial time improves the WRF water vapor initial structures, which improves the water vapor forecast performance primarily within

the beginning a few hours. We however use the results from 2 h UTC to 7 h UTC (WRF forecasting lead time of 2 h to 7 h) to analyze positioning results after carrier phase ambiguities have converged. When the lead time extends, assimilation of external water vapor data may lead to insignificant positive impacts or even negative impacts. As said, the assimilation of water vapor data into WRF model can help improve the WRF performance in the very beginning hours. The PPP carrier phase ambiguity resolution takes place in the beginning hours too. Therefore, we expect the WRF-augmented PPP with data assimilation should has a faster ambiguity convergence speed in the PPP early stage. The static PPP convergence time, analyzed in the next Section 5.2.2, confirms our analysis.

5.2.2 Static PPP Convergence Time

The time used for GNSS carrier phase ambiguity resolution, leading to static PPP solution convergence in the east, north, and up components, is an important factor in performance assessment. The convergence time is defined as the period from the first epoch of static PPP to the last epoch with a positioning error in a given component larger than the convergence criterion. The convergence criterion defined in this study is that positioning error is less than 10 cm in a given component.

The average convergence time for different WRF-augmented PPP schemes are summarized in Table 8. We can find that WRF-augmented PPP improves convergence speed in both north and up components. WRF-augmented PPP schemes 0-3 shorten the convergence time in up component by 47.1%, 57.3%, 43.3%, and 54.8%, respectively. The convergence time in the north component is reduced by up to 3.4% using different schemes. It is worth mentioning that WRF-augmented PPP scheme 1 (with GNSS PWV assimilation) and scheme 3 (with both GNSS PWV and radiosonde profiles assimilation) has a faster convergence speed than WRF-augmented PPP scheme 0 (without data assimilation). It implies that WRF schemes 1 and 3 provide more accurate wet delay corrections at the early stage of PPP calculation. This is expected and consistent with our analysis in the last paragraph of Section 5.2.1.

Table 8 Average convergence time in east, north, and up components in static PPP for seven IGS stations during April 06 to 11, 2020. Unit of convergence time: minutes. The convergence time in one component is defined as the last epoch in that component with a positioning error exceeding the defined convergence criterion. The convergence criterion is defined as10 cm in this study

	Estimated static PPP	WRF scheme 0	WRF scheme 1	WRF scheme 2	WRF scheme 3
East	8.6	9.4 (9.3%)	9.4 (9.3%)	9.7 (12.8%)	9.3 (8.1%)
North	2.9	2.8 (-3.4%)	2.8 (-3.4%)	2.8 (-3.4%)	2.9 (0%)
Up	15.7	8.3 (-47.1%)	6.7 (-57.3%)	8.9 (-43.3%)	7.1 (-54.8%)

6 Conclusions

We have conducted six consecutive 24-h WRF modeling by assimilating water vapor at 0 h UTC of each day from April 06, 2020 to April 11, 2020 in the South China region 20° N – 33° N and 108° E – 123° E. The WRF water vapor forecasting results are evaluated by GNSS-derived PWV. We then adopted the WRF forecast water vapor to augment the performance of GNSS static and kinematic PPP.

To obtain more accurate WRF water vapor forecasting results, we assimilate PWV from 27 China CMONOC GNSS stations and meteorological profiles from 22 radiosonde stations into WRF model with four data assimilation schemes, i.e. WRF scheme 0: WRF without data assimilation; WRF scheme 1: WRF with assimilation of GNSS PWV only; WRF scheme 2: WRF with assimilation of radiosonde profiles only; WRF scheme 3: WRF with assimilation of both GNSS PWV and radiosonde profiles.

The comparison of WRF forecast PWV with CMONOC GNSS PWV shows that assimilating GNSS PWV and radiosonde PWV can improve the accuracy of WRF PWV results with a forecasting lead time of 5-7 h. Without data assimilation into WRF, the RMSE of WRF PWV forecasting results within the first 7 h is 2.3 kg/m^2. With data assimilation into WRF, the RMSE of WRF schemes 1 to 3 are 1.9 kg/m^2, 2.3 kg/m^2 and 2.0 kg/m^2, respectively. The largest PWV accuracy improvement is 17.4% with WRF scheme 1.

Our results indicate that PPP-augmented by WRF forecast PWV improves the overall 3D positioning accuracy and convergence time, particularly in up component. The static PPP results show that the up component positioning errors are reduced by 42.3%, 29.5%, 40.6%, and 29.9% using WRF-augmented PPP schemes 0 to 3 respectively. The corresponding 3D positioning errors with WRF-augmented PPP schemes 0 to 3 are also reduced by 35.4%, 24.8%, 34.0%, and 25.5%. With the PWV augmentation from WRF forecasting schemes 0 to 3, the static PPP ambiguity convergence time is shortened by 47.1%, 57.3%, 43.3%, and 54.8%, respectively, using 10 cm as the convergence criterion.

The kinematic PPP results show that the up component positioning errors are reduced by 33.3%, 21.5%, 33.6%, and 20.0% using WRF-augmented PPP schemes 0 to 3, respectively. The 3D positioning errors for WRF-augmented PPP schemes 0 to 3 are reduced by 25.5%, 14.8%, 26.3%, and 14.8%, respectively.

The accuracy of WRF water vapor forecasting results is expected to be further improved if PWV data from more GNSS stations are assimilated into the WRF model. Consequently, the WRF-augmented static and kinematic PPP performances are expected to be further improved.

Acknowledgments

The support from the Key Program of the National Natural Science Foundation of China (No. 41730109) is acknowledged. The work described in this paper was also supported by a grant from the Research Grants Council of the Hong Kong Special Administrative Region, China (Project No. PolyU 15211919 Q73B). The Emerging Frontier Area (EFA) Scheme of Research Institute for Sustainable Urban Development (RISUD) of the Hong Kong Polytechnic University (No. 1-BBWJ) is also acknowledged. The authors thank GNSS data product service platform of China Earthquake Administration for providing GNSS PWV data of the Crustal Movement Observation Network Of China (CMONOC) (http://www.cgps.ac.cn). The National Oceanic and Atmospheric Administration (NOAA) is thanked for providing the Integrated Global Radiosonde Archive (IGRA) radiosonde data (ftp://ftp.ncdc.noaa.gov/pub/data/igra/). We thank online archives of the Crustal Dynamics Data Information System (CDDIS), NASA Goddard Space Flight Center, Greenbelt, MD, USA, for providing IGS GNSS data (https://cddis.nasa.gov/archive/gnss/data/daily/). The European Centre for Medium-Range Weather Forecasts (ECMWF) (https://cds.climate.copernicus.eu/#!/search?text=ERA5&type=dataset) is appreciated for providing the ECMWF ERA5 reanalysis data.

References

1. Kouba J, Héroux P (2001) Precise Point Positioning Using IGS Orbit and Clock Products. GPS Solutions 5:12–28
2. Liu T, Yuan Y, Zhang B, Wang N, Tan B, Chen Y (2017) Multi-GNSS precise point positioning (MGPPP) using raw observations. Journal of geodesy 91:253–268
3. Jin S, Su K (2020) PPP models and performances from single-to quad-frequency BDS observations. Satellite Navigation 1:1–13
4. Geng J, Teferle FN, Meng X, Dodson A (2011) Towards PPP-RTK: Ambiguity resolution in real-time precise point positioning. Advances in space research 47:1664–1673
5. Cai C, Gao Y (2013) Modeling and assessment of combined GPS/GLONASS precise point positioning. GPS solutions 17:223–236
6. Li X, Zhang X, Ren X, Fritsche M, Wickert J, Schuh H (2015) Precise positioning with current multi-constellation global navigation satellite systems: GPS, GLONASS, Galileo and BeiDou. Scientific reports 5:8328
7. Lu C, Li X, Zus F, Heinkelmann R, Dick G, Ge M, Wickert J, Schuh H (2017) Improving BeiDou real-time precise point positioning with numerical weather models. Journal of Geodesy 91:1019–1029
8. Tunalı E, Özlüdemir MT (2019) GNSS PPP with different troposphere models during severe weather conditions. GPS Solutions 23:82
9. Wang J, Liu Z (2019) Improving GNSS PPP accuracy through WVR PWV augmentation. Journal of Geodesy 93:1685–1705
10. Yao Y, Yu C, Hu Y (2014) A new method to accelerate PPP convergence time by using a global zenith troposphere delay estimate model. The Journal of Navigation 67:899–910

11. Yao Y, Peng W, Xu C, Cheng S (2017) Enhancing real-time precise point positioning with zenith troposphere delay products and the determination of corresponding tropospheric stochastic models. Geophys J Int 208:1217–1230
12. Zhang H, Yuan Y, Li W, Li Y, Chai Y (2016) Assessment of Three Tropospheric Delay Models (IGGtrop, EGNOS and UNB3m) Based on Precise Point Positioning in the Chinese Region. Sensors 16:122
13. Chen B, Liu Z (2016) A Comprehensive Evaluation and Analysis of the Performance of Multiple Tropospheric Models in China Region. IEEE Trans Geosci Remote Sens 54:663–678
14. Hadas T, Kaplon J, Bosy J, Sierny J, Wilgan K (2013) Near-real-time regional troposphere models for the GNSS precise point positioning technique. Measurement Science and Technology 24:055003
15. Zheng F, Lou Y, Gu S, Gong X, Shi C (2018) Modeling tropospheric wet delays with national GNSS reference network in China for BeiDou precise point positioning. Journal of Geodesy 92:545–560
16. Li Y, Zou X, Tang W, Deng C, Cui J, Wang Y (2020) Regional modeling of tropospheric delay considering vertically and horizontally separation of station for regional augmented PPP. Advances in Space Research 66:2338–2348
17. Liu Z, Li M, Zhong W, Wong MS (2013) An approach to evaluate the absolute accuracy of WVR water vapor measurements inferred from multiple water vapor techniques. Journal of Geodynamics 72:86–94
18. Powers JG, Klemp JB, Skamarock WC, et al (2017) The Weather Research and Forecasting Model: Overview, System Efforts, and Future Directions. Bulletin of the American Meteorological Society 98:1717–1737
19. Dullaart JC, Muis S, Bloemendaal N, Aerts JC (2020) Advancing global storm surge modelling using the new ERA5 climate reanalysis. Climate Dynamics 54:1007–1021
20. Hobiger T, Shimada S, Shimizu S, Ichikawa R, Koyama Y, Kondo T (2010) Improving GPS positioning estimates during extreme weather situations by the help of fine-mesh numerical weather models. Journal of Atmospheric and Solar-Terrestrial Physics 72:262–270
21. Ibrahim HE, El-Rabbany A (2011) Performance analysis of NOAA tropospheric signal delay model. Meas Sci Technol 22:115107
22. Wilgan K, Hadas T, Hordyniec P, Bosy J (2017) Real-time precise point positioning augmented with high-resolution numerical weather prediction model. GPS solutions 21:1341–1353
23. Hersbach H, Bell B, Berrisford P, et al (2020) The ERA5 global reanalysis. Quarterly Journal of the Royal Meteorological Society
24. Barker DM, Huang W, Guo Y-R, Bourgeois A, Xiao Q (2004) A three-dimensional variational data assimilation system for MM5: Implementation and initial results. Monthly Weather Review 132:897–914
25. Huang X-Y, Xiao Q, Barker DM, et al (2009) Four-dimensional variational data assimilation for WRF: Formulation and preliminary results. Monthly Weather Review 137:299–314
26. Leung LR, Qian Y (2009) Atmospheric rivers induced heavy precipitation and flooding in the western US simulated by the WRF regional climate model. Geophysical research letters 36:
27. Gao Y, Xu J, Chen D (2015) Evaluation of WRF mesoscale climate simulations over the Tibetan Plateau during 1979–2011. Journal of Climate 28:2823–2841
28. Kain JS (2004) The Kain–Fritsch convective parameterization: an update. Journal of applied meteorology 43:170–181
29. Iacono MJ, Delamere JS, Mlawer EJ, Shephard MW, Clough SA, Collins WD (2008) Radiative forcing by long-lived greenhouse gases: Calculations with the AER radiative transfer models. Journal of Geophysical Research: Atmospheres 113:
30. Hong S-Y, Noh Y, Dudhia J (2006) A new vertical diffusion package with an explicit treatment of entrainment processes. Monthly weather review 134:2318–2341

31. Jiménez PA, Dudhia J, González-Rouco JF, Navarro J, Montávez JP, García-Bustamante E (2012) A revised scheme for the WRF surface layer formulation. Monthly Weather Review 140:898–918
32. Dudhia J (1996) A multi-layer soil temperature model for MM5. In: Preprints, The Sixth PSU/NCAR mesoscale model users' workshop. pp 22–24
33. Mateus P, Nico G, Catalão J (2015) Uncertainty assessment of the estimated atmospheric delay obtained by a numerical weather model (NMW). IEEE Transactions on Geoscience and Remote Sensing 53:6710–6717
34. Askne J, Nordius H (1987) Estimation of tropospheric delay for microwaves from surface weather data. Radio Science 22:379–386
35. Rüeger JM (2002) Refractive index formulae for radio waves. Integration of techniques and corrections to achieve accurate engineering 19–26
36. Bevis M, Businger S, Chiswell S, Herring TA, Anthes RA, Rocken C, Ware RH (1994) GPS Meteorology: Mapping Zenith Wet Delays onto Precipitable Water. J Appl Meteor 33:379–386
37. Bevis M, Businger S, Herring TA, Rocken C, Anthes RA, Ware RH (1992) GPS meteorology: Remote sensing of atmospheric water vapor using the global positioning system. Journal of Geophysical Research: Atmospheres 97:15787–15801
38. Zhao Q, Yao Y, Yao W, Zhang S (2019) GNSS-derived PWV and comparison with radiosonde and ECMWF ERA-Interim data over mainland China. Journal of Atmospheric and Solar-Terrestrial Physics 182:85–92
39. Herring T, King R, McClusky S (2010) Documentation of the GAMIT GPS Analysis Software release 10.4. Department of Earth and Planetary Sciences, Massachusetts Institute of Technology, Cambridge, Massachusetts 1–171
40. Saastamoinen J (1972) Atmospheric Correction for the Troposphere and Stratosphere in Radio Ranging Satellites. Geophys Monogr Ser 15:247–251
41. Dach R, Lutz S, Walser P, Fridez P (2015) Bernese GNSS software version 5.2. University of Bern, Bern Open Publishing
42. Hu J, Zhang X, Li P, Ma F, Pan L (2020) Multi-GNSS fractional cycle bias products generation for GNSS ambiguity-fixed PPP at Wuhan University. GPS Solutions 24:1–13